SPE-182605-MS

Coupled Reservoir-Geomechanical Simulation of Caprock Failure and Fault Reactivation During CO_2 Sequestration in Deep Saline Aquifers

P. H. Winterfeld and Yu-Shu Wu, Colorado School of Mines

This paper was prepared for presentation at the SPE Reservoir Simulation Conference held in Montgomery, TX, USA, 20–22 February 2017.

Abstract

An aquifer suitable for underground carbon dioxide sequestration needs to be overlain by sealing caprock because carbon dioxide is less dense than the native brine and would tend to rise upward. This paper presents a thermal-hydrological-mechanical (THM) reservoir simulator that is applicable to assessing the sealing capability of such caprock. The geomechanical portion consists of an equation for mean stress, derived from linear elastic theory for a thermo-poro-elastic system, and equations for stress tensor components that depend on mean stress and other variables. The fluid and heat flow portion of our simulator is for general multiphase, multicomponent, multi-porosity systems. We add the capability of simulating caprock failure scenarios, namely tensile failure, fracture and fault reactivation, and shear failure, to the formulation. We then show simulation examples for code verification and demonstration of its capabilities, including a simulation of caprock leakage from carbon dioxide injection, a demonstration of the simulator's ability to predict of shear failure, and a simulation an experiment of pressure-induced fracturing of a concrete block that includes tensile failure.

Introduction

A promising option for reducing atmospheric anthropogenic carbon dioxide is to inject it underground into a deep saline aquifer. Although this carbon dioxide would be a super critical fluid when injected, it is still less dense than the native brine and would tend to rise upward. Thus, an aquifer suitable for underground carbon dioxide sequestration needs to be overlain by sealing caprock for the duration of the carbon sequestering process. A homogeneous caprock layer with a sufficiently small permeability would inhibit sequestered carbon dioxide from leaking through. However, geological systems often are heterogeneous and discontinuous, and may contain fractures and faults. Carbon dioxide injection pressurizes the reservoir, and this pressurization can reactivate existing faults and fractures and provide flow paths that allow leakage of carbon dioxide from the saline aquifer. In addition, if the pressurization is sufficiently high, the caprock can fracture.

A simulation model that can predict caprock failure and fault reactivation would be a useful tool in enhancing our ability to predict reservoir conditions, integrity, and enhance the performance of life cycle storage operations for carbon dioxide geologic storage. Such a model would couple fluid flow with geomechanics, as well as have criteria for caprock failure and fault reactivation. Examples of coupled fluid flow-geomechanical simulators that have been reported in the literature are TOUGH2-FLAC3D (Rutqvist et al., 2002), a linkage of TOUGH2, a well-established code for geohydrological analysis with multiphase, multicomponent fluid flow and heat transport, and FLAC3D, a widely used commercial code that is designed for rock and soil mechanics with thermomechanical and hydromechanical interactions; TOUGH–RDCA (Pan et al., 2014), a linkage of TOUGH2 and RDCA, developed for simulating the nonlinear and discontinuous geomechanical behavior of rock; CODE-BRIGHT (Olivella et al., 1996), a finite element code that simulates non-isothermal multiphase flow of brine and gas in deformable media; Code_Aster (Sayedi at al., 2009), a thermal-mechanical finite element code that was coupled to TOUGH2 to simulate thermo-hydro-mechanical processes under multiphase flow; FEHM (Bower and Zyvoloski, 1997), a coupled thermal-hydrologic-mechanical dual porosity finite element code that allows permeability of up to two perpendicular fracture planes vary with normal stress; and OpenGeoSys (Wang and Kolditz, 2007; Goerke et al., 2011), an object oriented open source thermal-hydrological-mechanical finite element code.

In this paper, we present a thermal-hydrologic-mechanical (THM) simulation model that can predict caprock failure and fault reactivation. A fully coupled THM simulator was presented by Winterfeld and Wu (2014) and Hu *et al*. (2013). In their approach, the geomechanical equations relating stresses and displacements were combined to yield an equation for mean stress, a primary variable, and volumetric strain, a rock property. This formulation was then extended by Winterfeld and Wu (2016) to calculate the stress tensor components efficiently and is the geomechanical formulation for our simulator. We begin by summarizing this geomechanical formulation, along with the associated fluid and heat flow formulation, and then present the formulation used to predict caprock failure and fault reactivation. Example problems are then used to provide verification of our technique, including a simulation of caprock leakage from carbon dioxide injection that is from the literature, a demonstration of the simulator's ability to predict of shear failure, and a simulation of an experiment of pressure-induced fracturing of a concrete block.

Simulator Fluid Flow and Geomechanical Formulation

Our simulator's geomechanical and fluid flow formulation has been described in detail in Winterfeld and Wu (2016) and is outlined here. The fluid flow formulation is based on the TOUGH2 one (Pruess et al., 1999) for general multiphase, multicomponent, multi-porosity systems. Fluid advection is described with a multiphase version of Darcy's law. Heat flow occurs by conduction and convection, the latter including sensible as well as latent heat effects. The description of thermodynamic conditions is based on the assumption of local equilibrium of all phases and rock media.

Our simulator's mean stress geomechanical formulation is based on the classical theory of elasticity extended to multi-porosity non-isothermal media (Winterfeld and Wu, 2014). Hooke's law for such a medium is given by:

$$\boldsymbol{\tau} - \left[\sum_j \left(\alpha_j P_j + 3\beta K \omega_j \left(T_j - T_{ref}\right)\right)\right]\mathbf{I} = 2G\boldsymbol{\varepsilon} + tr\left(\boldsymbol{\varepsilon}\right)\lambda\mathbf{I} \tag{1}$$

where G is shear modulus, λ is the Lamé parameter, the summation is over multi-porosity continua, α is Biot's coefficient, T_{ref} is reference temperature for a thermally unstrained state, β is linear thermal expansion coefficient, K is bulk modulus, and ω is porous continuum volume fraction.

Two other fundamental relations in the theory of linear elasticity are the relation between the strain tensor and the displacement vector $\mathbf{u}$:

$$\boldsymbol{\varepsilon} = \frac{1}{2}\left(\nabla\mathbf{u} + \nabla\mathbf{u}^t\right) \tag{2}$$

and the static equilibrium equation:

$$\nabla \cdot \boldsymbol{\tau} + \mathbf{F}_b = 0 \tag{3}$$

where $\mathbf{F}_b$ is the body force. We combine Equations 1-3 to obtain the thermo-multi-poroelastic Navier equation:

$$\nabla\left[\sum_j \left(\alpha_j P_j + 3\beta K \omega_j T_j\right)\right] + (\lambda + G)\nabla(\nabla \cdot \mathbf{u}) + G\nabla^2 \mathbf{u} + \mathbf{F}_b = 0 \tag{4}$$

We then take the divergence of Equation 4 to yield an equation relating mean stress, pore pressures, and temperatures (Winterfeld and Wu, 2014):

$$\nabla \cdot \left[\frac{3(1-\upsilon)}{1+\upsilon}\nabla \tau_m + \mathbf{F}_b - \frac{2(1-2\upsilon)}{1+\upsilon}\nabla\left(\sum_j \left(\alpha_j P_j + 3\beta K \omega_j T_j\right)\right)\right] = 0 \tag{5}$$

where τ_m is mean stress and υ is Poisson's ratio. In addition, the trace of the stress tensor is an invariant and yields a relation between volumetric strain and mean stress, pore pressures, and temperatures:

$$K\varepsilon_v = \tau_m - \sum_j \left(\alpha_j P_j + 3\beta K \omega_j \left(T_j - T_{ref}\right)\right) \tag{6}$$

where ε_v is volumetric strain. We couple fluid and heat flow to geomechanics by solving Equation 5 along with the mass and energy conservation equations arising from the fluid and heat flow formulation, with mean stress as an additional primary variable and volumetric strain as an additional property.

We calculate stress tensor components after solving for mean stress, pressures, temperatures, and mass fractions. The normal stress tensor component in the k-direction, x_k, is obtained by taking the k-direction derivative of component k of Equation 4:

$$\frac{\partial^2}{\partial x_k^2}\left[h(\mathbf{P},\mathbf{T})\right] + \frac{3}{2(1+\upsilon)}\frac{\partial^2}{\partial x_k^2}\left(\tau_m - h(\mathbf{P},\mathbf{T})\right) + \frac{1}{2}\nabla^2\left(\tau_{x_k x_k} - h(\mathbf{P},\mathbf{T}) - \frac{3\upsilon}{1+\upsilon}\left(\tau_m - h(\mathbf{P},\mathbf{T})\right)\right) + \frac{\partial}{\partial x_k}F_{b,x_k} = 0 \tag{7}$$

where

$$h(\mathbf{P},\mathbf{T}) = \sum_j \left(\alpha_j P_j + 3\beta K \omega_j \left(T_j - T_{ref}\right)\right) \tag{8}$$

The shear stress tensor component in the k- and l-directions is obtained by averaging the k-direction derivative of component l of Equation 4 and the l-direction derivative of component k of Equation 4:

$$\frac{\partial^2}{\partial x_k \partial x_l}\left[h(\mathbf{P},\mathbf{T})\right] + \frac{3}{2(1+\upsilon)}\frac{\partial^2}{\partial x_k \partial x_l}\left(\tau_m - h(\mathbf{P},\mathbf{T})\right) + \frac{1}{2}\nabla^2 \boldsymbol{\tau}_{x_k x_l} + \frac{1}{2}\left(\frac{\partial}{\partial x_k}F_{b,x_l} + \frac{\partial}{\partial x_l}F_{b,x_k}\right) = 0 \tag{9}$$

The fluid and heat flow and geomechanical equations are discretized in space on a Cartesian grid and solved using the integral finite difference method (Narasimhan and Witherspoon, 1976). Conservation of mass, energy, and the mean stress equation are solved simultaneously first. Normal and shear stresses appearing in those equations are evaluated at the previous time step and the rest of the primary variables are evaluated at the current time step. The normal and shear stress equations are solved next. Normal and shear stresses that do not appear in the Laplacian terms are evaluated at the previous time step, and all other instances of primary variables are evaluated at the current time step.

Our simulator is massively parallel, with domain partitioning using the METIS and ParMETIS packages (Karypsis and Kumar, 1998; Karypsis and Kumar, 1999). Each processor computes Jacobian matrix elements for its own grid blocks and exchange of information between processors uses MPI (Message Passing Interface) and allows calculation of Jacobian matrix elements associated with inter-block connections across domain partition boundaries. The Jacobian matrix is solved in parallel using an iterative linear solver from the Aztec package (Tuminaro *et al*. 1999).

Caprock Failure Scenarios

In this section, caprock failure scenarios that are incorporated into our simulator are described. There are three, with the first being tensile failure of caprock from excess pressurization, the second fault reactivation, and the third shear failure of a fault or caprock.

Tensile Failure

Caprock can undergo tensile failure when pressurization from CO_2 injection becomes too large. A common assumption (for example, Chin et al. (2009) and Rutqvist et al. (2008)) is that tensile failure could occur when the fluid pressure exceeds the least compressive principal stress. Such an assumption, a conservative one, is based on the notion that the grain-grain interfaces in the caprock have negligible tensile strength and those interfaces will break as soon as the effective stress, the difference between the directional applied stress and the pore pressure, in one direction becomes zero. In our simulator, we include a more general caprock tensile failure criterion that allows for non-zero the tensile strength:

$$P \geq \sigma_3 + \sigma_{tn} \tag{10}$$

where σ_{m} is tensile strength and where σ_3 is the least compressive principal stress. We apply Equation 10 to each grid block. When Equation 10 becomes satisfied, we then conceptualize the initialization of a single uniform fracture, perpendicular to the minimum principle stress direction, in the grid block. We estimate the width of this fracture using a simple model, based on the two-dimensional Perkins-Kern (1961) fracture model, and used by Goodarzi et al. (2012) and Settari and Warren (1994) to couple dynamic fracture propagation to fluid flow and geomechanics:

$$w_{fr} = \frac{4(1-\upsilon^2)h_{fr}}{E}\left(P - \sigma_3\right) \tag{11}$$

where E is Young's modulus, v is Poisson's ration, h_{fr} is the fracture half height, w_{fr} is the fracture width. The initialization of this fracture modifies the grid block permeability and porosity. We model porosity by lumping the pore volume associated with the newly initialized fracture with the pore volume of the rest of the grid block (the grid block matrix) to yield an overall effective porosity:

$$\phi = \frac{w_{fr}A_{fr} + V_m\phi_m}{w_{fr}A_{fr} + V_m} \approx \phi_m + \frac{w_{fr}A_{fr}}{V_m} \tag{12}$$

where A_{fr} is the fracture face area and m refers to the grid block matrix. We model permeability by conceptualizing flow as occurring through both the fracture and the grid block matrix. For flow orthogonal to the principle minimum stress direction, we average the fracture and grid block matrix permeabilites in series with cross sectional area weighting:

$$k_k = \frac{k_{fr}w_{fr}\Delta x_{lj} + k_m \Delta x_l \Delta x_j}{\Delta x_{lj} + \Delta x_l \Delta x_j} \tag{13}$$

where k, l, and j each refer to a Cartesian direction, Δx is grid block length, and Δx_{lj} is the height of the fracture when projected into the lj-face. Permeability is unchanged for flow along the principle minimum stress direction, since fracture permeability is assumed to be much greater than the grid block matrix permeability. Fracture permeability is obtained from the well known expression for laminar flow through a slit:

$$k_{fr} = \frac{w_{fr}^2}{12} \tag{14}$$

Continued injection of fluid would cause the fracture width to increase and the fracture to extend. We allow fractures to extend into neighboring grid blocks that do not contain one. We track the fracture front position for connections between a grid block that contains a fracture and its neighbors that are in the direction a fracture would propagate, i.e. the perpendicular to the minimum stress direction. When this front encompasses the neighboring grid block, a fracture is initiated there. The criterion for the movement of a fracture front is given by Mastrojannis et al. (1980), who correlated the velocity of the extending fracture front as:

$$v = C\left(\frac{K_I - K_{IC}}{K_{IC}}\right)^n \tag{15}$$

where C and n are parameters that depend on the medium, K_{IC} is rock toughness, and K_I is stress intensity factor at the fracture tip. Yew (2015) gives an expression for this stress intensity factor:

$$K_I = \frac{E}{8\left(1-\upsilon^2\right)}\left(\frac{2\pi}{r}\right)^{\frac{1}{2}} w_{fr}(r) \tag{16}$$

where r is distance from the fracture front. We evaluate stress intensity factor using the fracture width calculated from Equation 11 and the grid block half dimension along the direction of fracture front propagation as the distance r from the fracture front.

Fault and Fracture Reactivation

Faults are complex systems consisting of a relatively thin inner core zone that has low permeability, surrounded by a fractured damage zone (Wibberly et al., 2009). Injection into a reservoir containing faults would alter the stress and pressure fields and can change the flow properties of a fault, such as increasing its ability to transmit fluid (reactivation). We approximate the faulted or fractured caprock region as consisting of a network of fractures that may be randomly oriented or have a preferred direction. The permeability and porosity of this region can change with changes in the stress and pressure fields, and we generalize these dependences as:

$$\phi = \phi\left(\boldsymbol{\tau}, P\right) \tag{17}$$

and

$$k_j = k_j\left(\boldsymbol{\tau}, P\right) \tag{18}$$

where subscript j refers to a Cartesian direction (j=1,2, or 3). One instance of such dependence is from Rutqvist et al. (2002), which conceptualized the fractured medium as an array of cubic blocks with the fractures being the interfaces between them. These fractures are equally spaced and oriented normal to each Cartesian direction. A fracture aperture is associated with each interface and correlations for fracture porosity and permeability were based on those apertures:

$$\phi = \phi_0 \frac{\sum_i b_i}{\sum_i b_{i,0}} \tag{19}$$

and

$$k_j = k_{j,0} \frac{\sum_{i \neq j} b_i^3}{\sum_{i \neq j} b_{i,0}^3} \tag{20}$$

where b_i is fracture aperture in direction i, k_j is permeability in direction j, and subscript 0 refers to a reference condition where permeability, porosity, and fracture aperture are specified. The dependence on aperture cubed in the permeability correlation results from the representation of flow through the fractures as that through a thin slit.

Fracture aperture is correlated with normal effective stress according to:

$$b_i = b_{i,r} + b_{i,\max} e^{-d_i \sigma_i^{'}} \tag{21}$$

where subscript r refers to a high effective stress residual aperture, subscript max refers to the maximum aperture increase at zero normal effective stress, and d is a parameter.

Shear Failure

Faults or weak zones in caprock can undergo shear failure when the shear stress acting on a caprock plane plane exceeds its shear strength. The most common shear failure criterion is the Coulomb (1773) one. Shear failure is likened to a sliding mass on a plane. The forces acting on the mass are friction, which resists sliding, and is given by its weight multiplied by a factor, and a force exerted on the mass in the direction of the plane that causes it to slide. For the Coulomb criteria, the sliding force is the shear stress on the caprock plane, the frictional force is the normal stress on the caprock plane, and an additional term is added that represents the cohesive strength of the material. In addition, when applied to poroelastic media, the normal stress is relaced by the effective normal stress (Terzaghi, 1936):

$$\tau = C_0 + \mu \sigma' \tag{22}$$

where C_0 is the cohesion and μ is the coefficient of internal friction. If the orientation of the caprock plane is specified, such as when considering a fault with a given orientation, the stress acting on that plane can be obtained by taking the dot product of the effective stress tensor with that plane's normal vector. That stress has components normal to that plane (the normal effective stress in Equation 22) and along that plane (the shear stress in Equation 22). For cases in which there is no specified plane, for example caprock containing randomly oriented fractures, shear failure would occur when the shear and effective normal stresses acting on any plane in the caprock satisfies Equation 22. These effective normal and shear stresses are obtained from the well known Mohr circle (Jaeger et al., 2007), which in equation form is:

$$\sigma' = \frac{(\sigma_1' + \sigma_3')}{2} + \frac{(\sigma_1 - \sigma_3)}{2} \cos 2\theta \tag{23}$$

and

$$\tau = -\frac{(\sigma_1 - \sigma_3)}{2} \sin 2\theta \tag{24}$$

where subscript 1 refers to the maximum principal stress, subscript 3 refers to the minimum principal stress, and θ is the angle measured from the first principal stress direction. Shear failure can be represented graphically as the intersection of the Mohr circle (Equations 23 and 24) with the Coulomb criterion, Equation 22, shown in Figure 1.

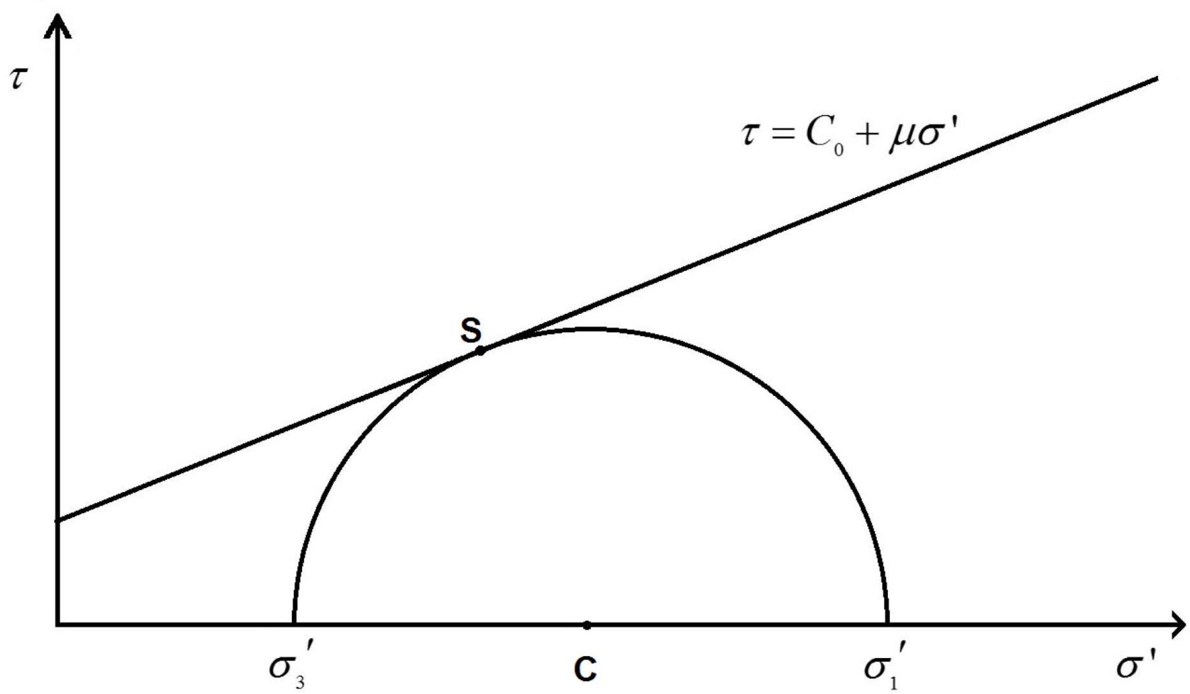

Figure 1—Mohr-Coulomb failure diagram in shear stress-normal effective stress space, with the Mohr circle centered at point "C" and failure line tangent to Mohr circle at point "S" when shear failure would occur. The Mohr circle range is from the minimum normal effective stress (subscript 3) to the maximum (subscript 1).

Shear failure may be accompanied by irreversible mechanical changes, including activating old fractures, forming new ones, as well as wave propagation, ground motion, and even earthquakes (Haring et al., 2008). The prediction of shear failure is simulated in our model; however, since our geomechanical formulation is based on an elastic medium, the simulation of these irreversible mechanical changes is beyond the scope of it.

Simulation Examples

We show simulation examples for code verification and demonstration of simulator capabilities. The first example is a simulation of caprock leakage resulting from carbon dioxide injection. This example is from the literature and we match some simulation results and demonstrate the simulator's prediction of shear failure. We then run a variant of that problem where we simulate normal effective stress dependence of fracture permeability and porosity. Finally, we simulate an experiment of pressure-induced fracturing of a concrete block that includes tensile failure.

CO_2 Leakage through Fault Zones

Rinaldi at al. (2014) studied fault responses during underground carbon dioxide injection, and focused on the short-term integrity of the sealing caprock and the potential for leakage. They considered stress/strain-dependent permeability and studied leakage through a fault zone as its permeability changes during reactivation. We ran some of their simulations using our model. Their "Scenario 1" (Mazzoldi et al., 2012) was a two-dimensional system with a minor 1 km fault that intersected a 100 m thick injection aquifer bounded above and below by a 150 m thick low-permeability caprock, shown in Figure 2, with rock properties shown in Table 1. Permeability and porosity depend on effective stress and is given by (Rutqvist and Tsang, 2002; Davies and Davies, 2001):

$$\phi = \phi_1 + \left(\phi_0 - \phi_1\right) e^{-\alpha\sigma'} \tag{25}$$

$$k = k_0 e^{c\left(\frac{\phi}{\phi_0}-1\right)} \tag{26}$$

where ϕ_0 is zero effective stress porosity, ϕ_1 is high effective stress porosity, exponent a is a parameter, constrant c is a parameter, and k_0 is zero effective stress permeability.

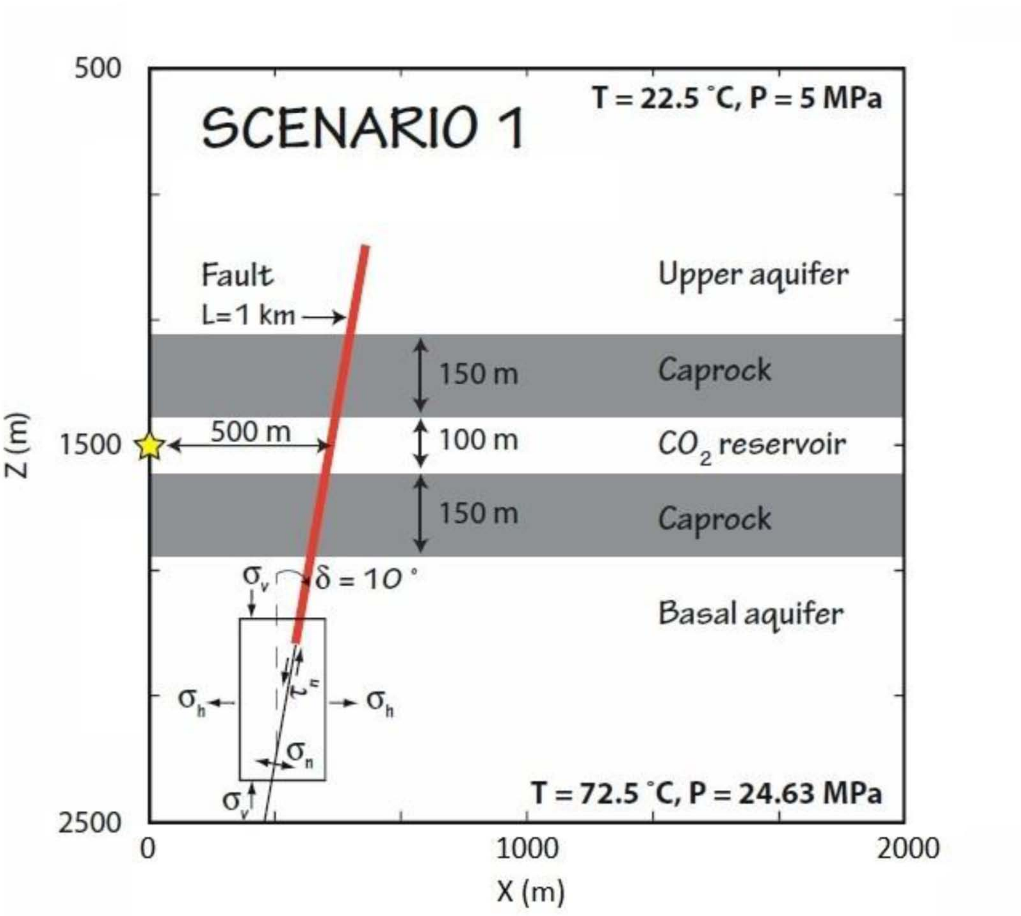

Figure 2—Schematic of "Scenario 1," adapted from Rinaldi et al. (2014), showing rock layers and fault. Injection site starred point at 1500 m depth.

Table 1—Rock properties used aquifer-caprock system.

Property\Layer	Upper	Caprock	CO_2 reservoir	Basal	Fault
Young's modulus, GPa	10.0	10.0	10.0	10.0	5.0
Poisson's ratio	0.25	0.25	0.25	0.25	0.25
Porosity	0.10	0.01	0.10	0.01	0.10
Permeability, m^2	10^{-14}	10^{-19}	10^{-13}	10^{-16}	10^{-14}-10^{-16}
Residual CO_2 saturation	0.05	0.05	0.05	0.05	0.05
Residual liquid saturation	0.3	0.3	0.3	0.3	0.3
Van Genuchten (1980) p0, kPa	19.9	621	19.9	621	19.9
Van Genuchten (1980) m	0.457	0.457	0.457	0.457	0.457

We simulated this system using a 190x145 grid. Grid block x-direction length was 20 m, except for the x-direction interval the fault was located in where it was 2 m. Grid block y-direction length was 20 m, except for the CO_2 reservoir and caprock layers where it was 10 m. The fault was represented by a series of connected grid blocks that approximate lie on the fault line shown in Figure 2. We ran two cases, the first with fault permeability 10^{-14} m^2 and CO_2 injection rate of 0.10 kg/sec-m, and the second with fault permeability 10^{-16} m^2 and CO_2 injection rate of 0.02 kg/sec-m, for five years. Figures 3 and 4 compare our fault permeability change at one and five years to those from the reference. There is good qualitative agreement between the two.

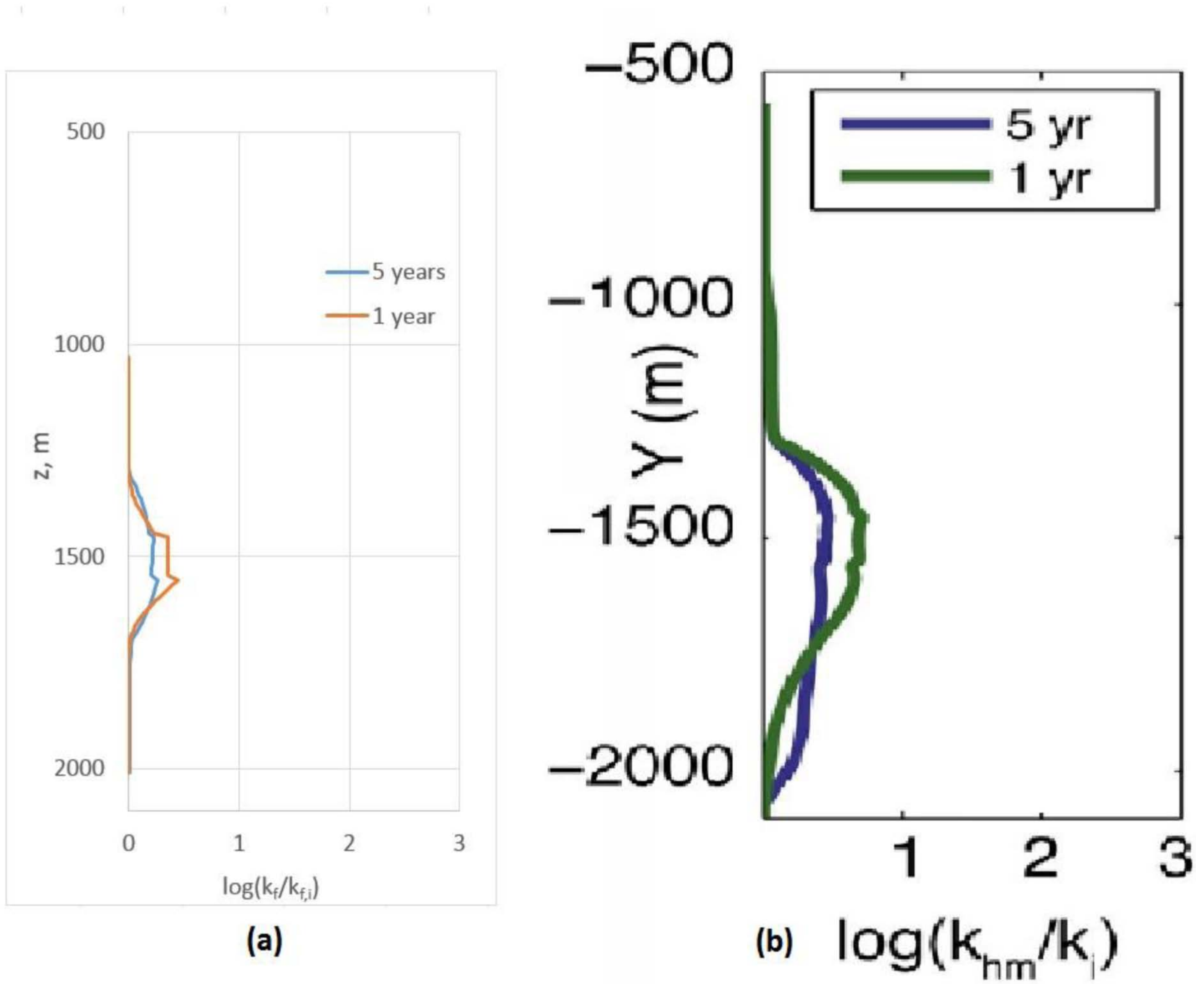

Figure 3—Fault permeability increase for our simulation (a) and reference (b) for fault permeability of 10^{-14} m^2 and CO_2 injection rate of 0.10 kg/sec-m.

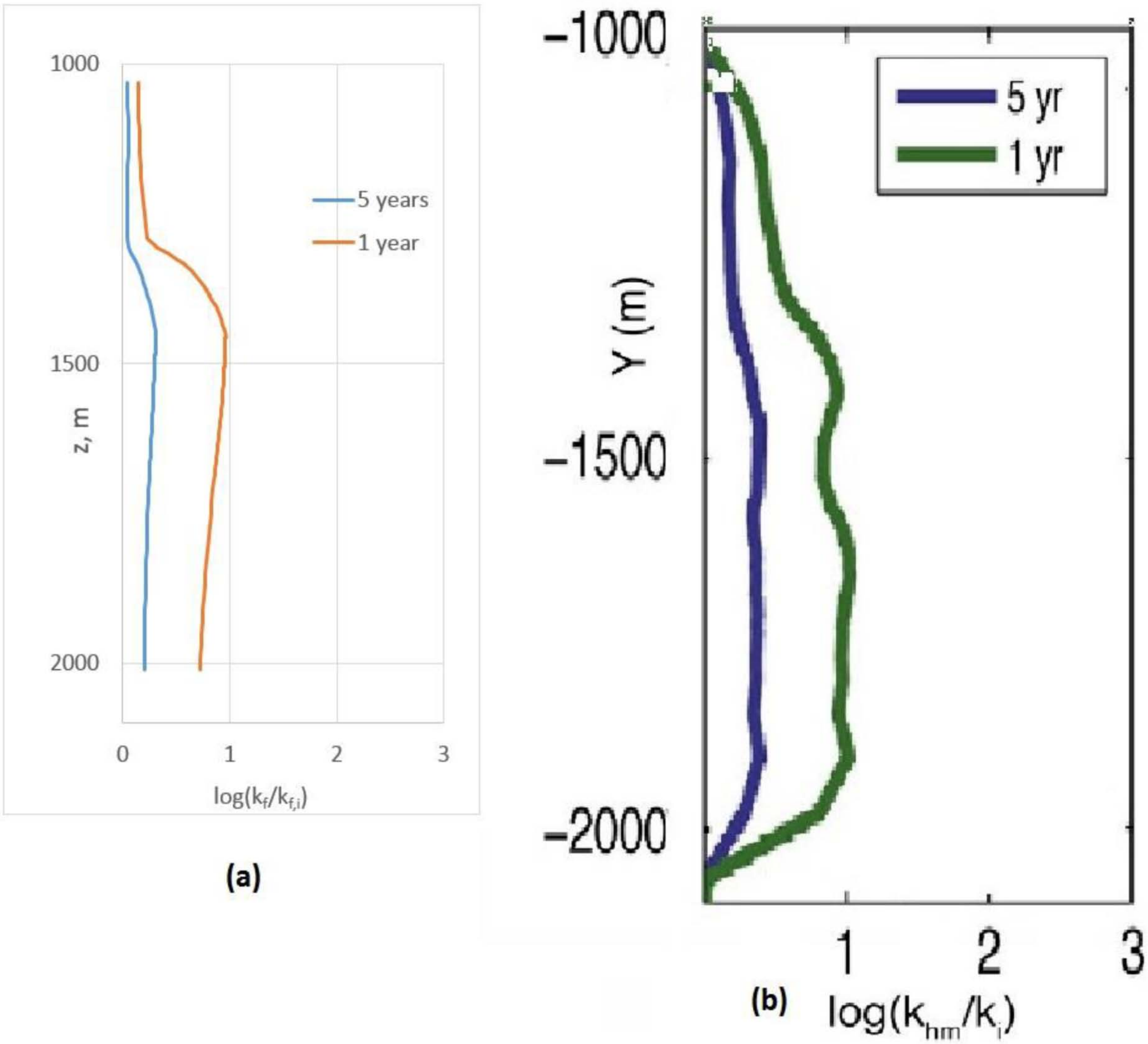

Figure 4—Fault permeability increase for our simulation (a) and reference (b) for fault permeability of 10^{-16} m^2 and CO_2 injection rate of 0.02 kg/sec-m.

We also ran this simulation with a Mohr-Coulomb failure envelope to demonstate that capability of the simulator to predict where shear failure of the fault could occur. The cohesion was zero and the coefficient of internal friction was 0.6. Figure 5 shows the predicted failure regions at varying times. These regions only lie along the fault; those outside the fault are not subject to shear failure.

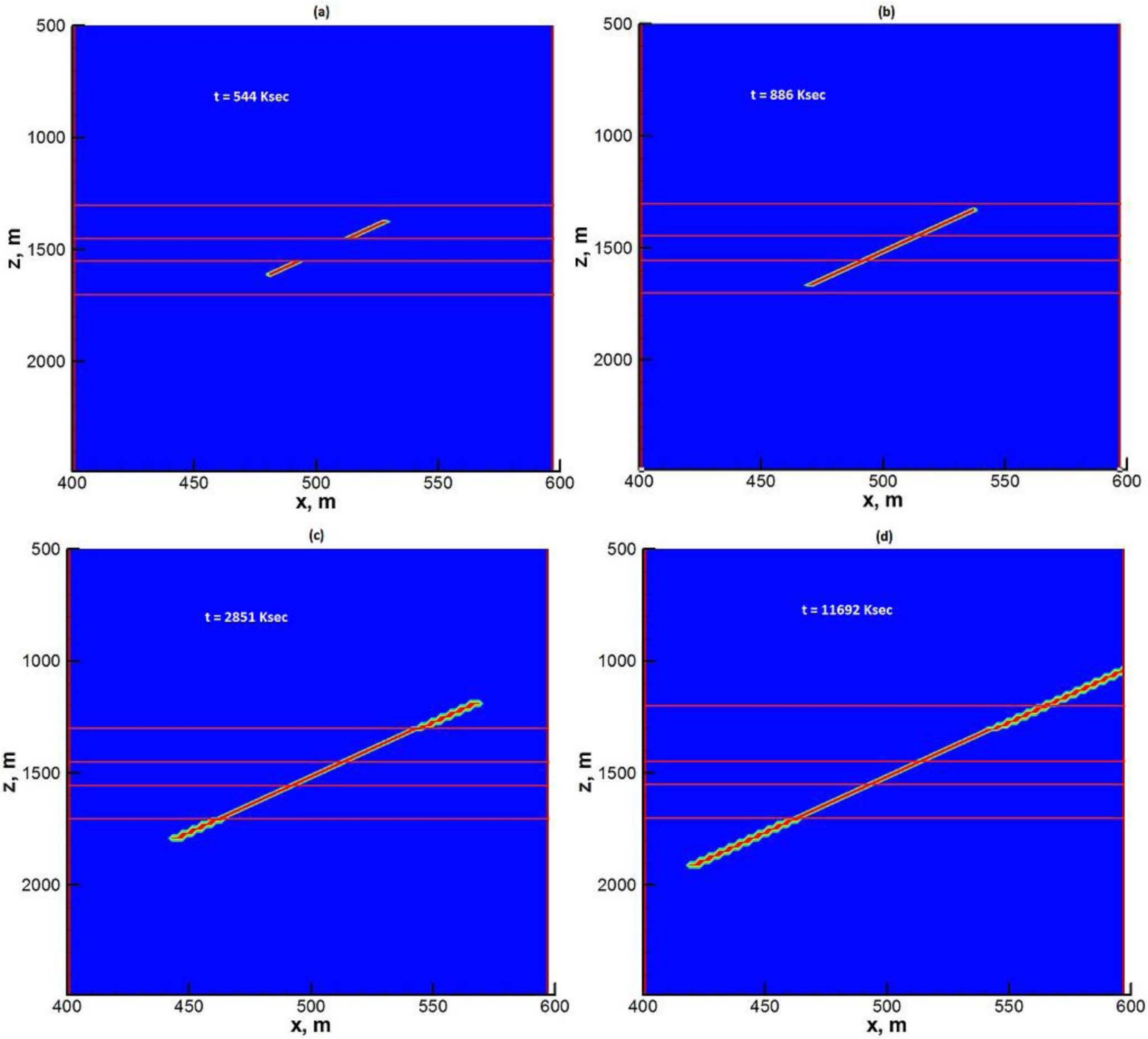

Figure 5—Mohr-Coulomb failure regions in fault shown at varying times: a) 544Ksec, b) 886 Ksec, c) 2851 Ksec, d) 11692 Ksec.

We ran a variant of this problem to demonstrate the calculation of permeability and porosity as a function of normal stress for a fractured medium (Equations 20-22). The previous fault was changed to a vertical one located at x-direction 500 m and whose z-direction range is from 1000 to 2000 m, and represented by a column of grid blocks. The fault permeability in the z-direction depends on normal stress and since the fault is vertical, it depends on the normal x-direction stress component. Fault permeability in the x-direction does not change. We reran the case with fault permeability 10^{-14} m^2 and CO_2 injection rate of 0.10 kg/sec-m for five years. Figure 6 shows the gas saturation at 1- and 5-years and Figure 7 shows the permeability increase at those times.

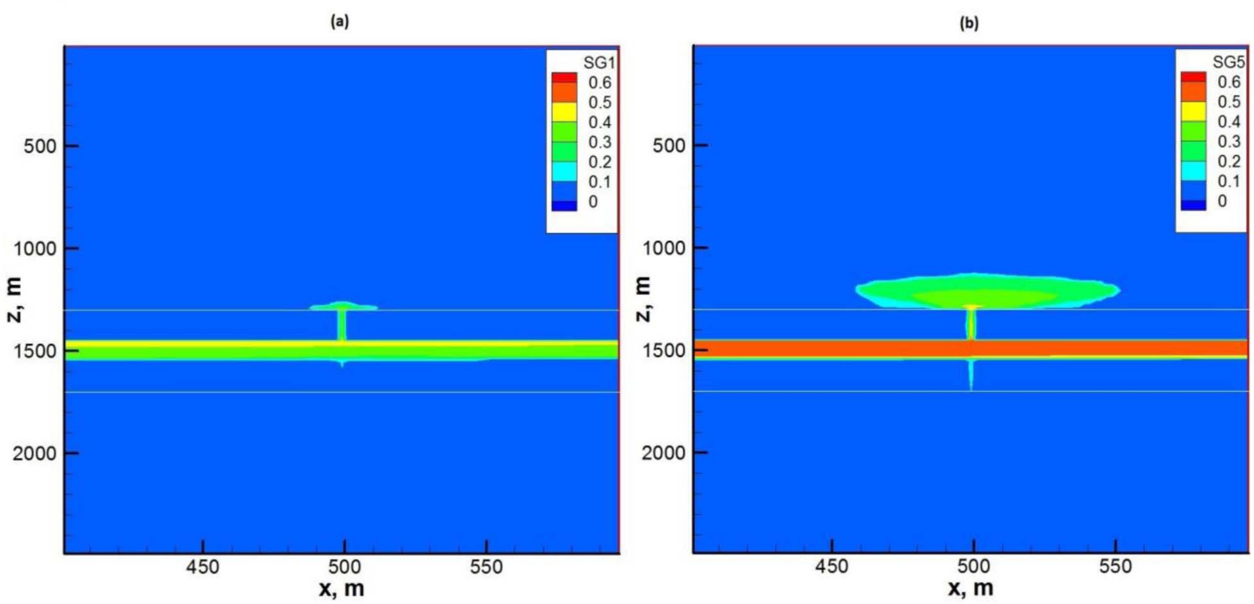

Figure 6—Gas saturation at one and five years. The white lines denote the boundaries between rock regions and the 1 km fracture, located at x=500m, is centered at z=1500m.

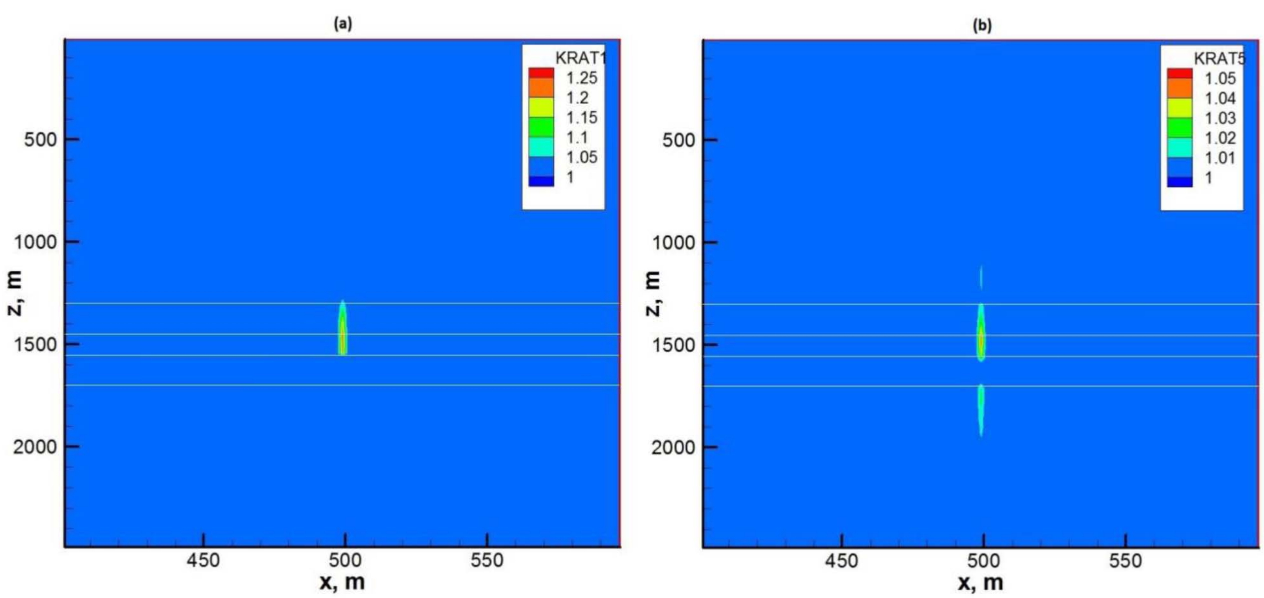

Figure 7—Permeability ratio at one and five years. The white lines denote the boundaries between rock regions and the 1 km fracture, located at x=500m, is centered at z=1500m.

Fracture of a Concrete Block

In order to develop a fundamental understanding of CO2 injection pressure-induced fracturing, we are doing laboratory studies using concrete representations of caprock to determine the correlations between confining stress, fluid pressure and fracturing initialization during CO2 injection. The equipment used for conducting these experiments includes a tri-axial loading system, an injection pump, and data acquisition devices. Initially, we use injected brine to identify the critical stress needed to initiate fractures in these caprock representations, which are 8 inch cubes that are cored in the center to create a 6 inch bore hole. We simulate one of these experiments, called "Sample 39" (Wu and Winterfeld, 2016). The cube initially contains a gaseous phase and its properties are shown in Table 2. The bore hole is simulated as a porous medium with much higher permeability than the surrounding concrete.

Table 2—Properties for brine injection experiment.

	Concrete	Bore hole
Young's modulus, GPa	6.0	6.0
Poisson's ratio	0.2	0.2
Porosity	0.10	0.90
Permeability, m^2	$1.0 \cdot 10^{-15}$	$1.0 \cdot 10^{-14}$
Biot's coefficient	1.0	0.0
Tensile strength, MPa	2.0	—
Toughness, MPa	0.1	—
Fracture extension A, m/sec	10.0	—
Fracture extension n	1.0	—

The confining stresses are 1000 psi in x-direction, 1500 psi in y-direction, and 2000 psi in z-direction. The lateral boundaries are at constant pressure and brine is injected at 40 ml/min uniformly along the lower half of the bore hole. The 11x11x11 grid is uniform in size. Since the minimum confining stress is in the x-direction, the concrete block will fracture in the yz-plane that contains the bore hole. We allow fracturing to occur only in that plane, which has the x-direction index of 6 in the grid. Figure 8 shows the simulated fracture at a time of 531 seconds. The fracture is initiated along the bore hole and extends outward. After the experiment is completed, the concrete block is dyed and broken apart by nitrogen in order to reveal the fracture induced by fluid injection. Figure 9 shows the result of this. The fracture is shown by the darker zone that extends a distance from the bore hole. The simulated fracture is somewhat similar to the experiment in that the overall fracture extents are similar. The simulation is a highly idealized representation of this process and is not expected to match the experiment in detail. For example, the fracture obtained by the experiment is not symmetrical about the bore hole whereas the simulation must be due to the nature of the data input (constant rock properties, and symmetry about the bore hole).

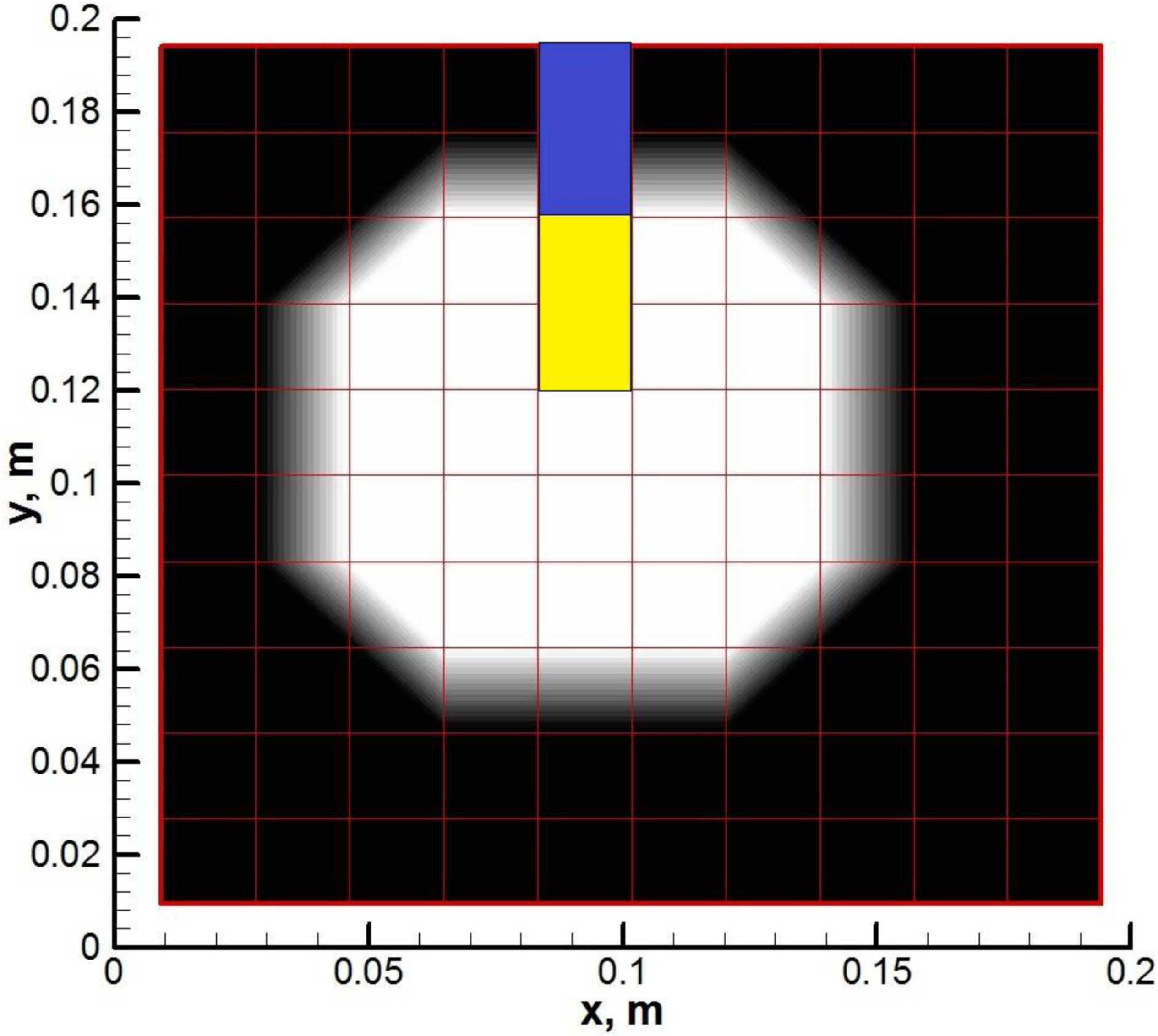

Figure 8—Simulated fracture of concrete block. White indicates fracture, bore hole is in yellow and blue, with yellow the perforated region and blue unperforated.

Figure 9—Internal fracture morphology of concrete sample after dyeing and gas breakdown.

Summary and Conclusions

We developed a thermal-hydrological-mechanical (THM) reservoir simulator that is applicable to assessing the sealing capability of caprock. The geomechanical portion consists of an equation for mean stress, derived from linear elastic theory for a thermo-poro-elastic system, and equations for stress tensor components that depend on mean stress and other variables. The fluid and heat flow portion of our simulator is for general multiphase, multicomponent, multi-porosity systems. We added the capability of simulating caprock failure scenarios, namely tensile failure, fracture and fault reactivation, and shear failure, to the formulation.

We verified our code by simulating of caprock leakage from carbon dioxide injection and matching published results. In addition, we demonstrated its capabilities by simulating shear failure, the normal effective stress dependence of fracture permeability and porosity, and an experiment of pressure-induced fracturing of a concrete block that includes tensile failure.

Acknowledgement

This work was supported by the Foundation CMG, the EMG of the Colorado School of Mines, and by the National Energy Technology Laboratory of the U. S. Department of Energy.

Nomenclature

a = parameter
A = area, L^2, m^2
b = fracture aperture, m
c = parameter
C = fracture propagation velocity parameter, L/t, m/s
C_0 = cohesion, m/Lt^2, Pa
$\boldsymbol{F}_\mathbf{b}$ = body force, mL/t^2, $kg\text{-}m/s^2$
G = shear modulus, m/Lt^2, Pa
h_{fr} = fracture half height, m
$\boldsymbol{I}$ = identity matrix
k = permeability, L^2, m^2
K = bulk modulus, m/Lt^2, Pa
K_I = stress intensity factor, m/Lt^2, Pa
K_{IC} = toughness, m/Lt^2, Pa
n = fracture propagation velocity parameter
P = pressure, m/Lt^2, Pa
T = temperature, T, K
T_{ref} = reference temperature, T, K
$\boldsymbol{u}$ = displacement vector, L, m
v = velocity, L/t, m/s
V = volume, L^3, m^3
w_{fr} = fracture width, m

Greek

α = Biot's coefficient
β = linear thermal expansion coefficient, 1/T, 1/K
$\boldsymbol{\varepsilon}$ = strain tensor
ε_v = volumetric strain

λ = Lamé parameter, m/Lt^2, Pa
μ = coefficient of internal friction
ν = Poisson's ratio
σ_1 = maximum principal stress, m/Lt^2, Pa
σ_3 = minimum principal stress, m/Lt^2, Pa
σ_{tn} = tensile strength, m/Lt^2, Pa
σ' = effective stress, m/Lt^2, Pa
$\boldsymbol{\tau}$ = stress tensor, m/Lt^2, Pa
τ_m = mean stress, m/Lt^2, Pa
τ = shear stress, m/Lt^2, Pa
ϕ = porosity
ω = volume fraction

Subscripts

fr = fracture
m = matrix
0 = reference

References

Bower, K. M., Zyvoloski, G. 1997. A numerical model for thermohydro-mechanical coupling in fractured rock. *Int J Rock Mech Min Sci* **34**:1201–1211

Chin, L.Y., Tomberlin, T.A., Ramos, G.G., and Chalaturnyk, R.J. 2012. Evaluation of Caprock Stability by Coupled Modeling of Geomechanics and Reservoir Simulation under Steam Injection for Producing Oil Sands Reservoirs, ARMA-2012-139. 46th U.S. Rock Mechanics/Geomechanics Symposium, 24-27 June, Chicago, Illinois.

Coulomb, C. A. 1773. Application des règles de maxima et minima à quelques problems de statique relatifs à l'Architecture [Application of the rules of maxima and minima to some problems of statics related to architecture], *Acad. Roy. Sci. Mem. Math. Phys*. **7**: 343–382.

Davies, J.P., Davies, D.K., 2001. Stress-dependent permeability: characterization andmodeling. *SPE J*. **6**, 224–235

Goerke U. J., Park, C. H., Wang, W., Singh, A. K., and Kolditz, O. 2011. Numerical simulation of multiphase hydromechanical processes induced by CO2 injection into deep saline aquifers. *Oil Gas Sci Technol Rev IFP* **66**:105–118

Häring, M. O., Schanz, U., Ladner, F., and Dyer, B. C. 2008. Characterisation of the basel 1 enhanced geothermal system. *Geothermics* **37**:469–495.

Jaeger, J. C., Cook, N. G. W., and Zimmerman, R. W. 2007. *Fundamentals of Rock Mechanics*. Malden, MA: Blackwell Publishing.

Karypis, G. and Kumar, V. 1998. A Parallel Algorithm for Multilevel Graph Partitioning and Sparse Matrix Ordering. *Journal of Parallel and Distributed Computing*. **48**: 71–85.

Karypis, G. and Kumar, V. 1999. A Fast and High Quality Multilevel Scheme for Partitioning Irregular Graphs. *Siam J. Sci. Comput*. **20** (1): 359–392.

Mastrojannis, E. N., Keer, L. M., and Mura, T. 1980. Growth of planar cracks induced by hydraulic fracturing. *International Journal for Numerical Methods in Engineering*. **15**: 41–54.

Mazzoldi, A., Rinaldi, A.P., Borgia, A., Rutqvist, J., 2012. Induced seismicity withingeological carbon sequestration projects: maximum earthquake magnitude andleakage potential from undetected faults. *Int. J. Greenhouse Gas Control* **10**, 434–442.

Narasimhan, T. N. and Witherspoon, P. A. 1976. An Integrated Finite Difference Method for Analysis of Fluid Flow in Porous Media. *Water Resources Res*. **12**: 57–64.

Olivella S., Carrera J., Gens A., and Alonso, E. E. 1994. Nonisothermal multiphase flow of brine and gas through saline media. *Trans Porous Media* **15**:271–293.

Pan, P.-Z., J. Rutqvist, X.-T. Feng, and F. Yan. 2014. An Approach for Modeling Rock Discontinuous Mechanical Behavior under Multiphase Fluid Flow Conditions. *Rock Mechanics and Rock Engineering*, **47**: 589–603.

Perkins, T.K., Kern, L.R., 1961. Widths of hydraulic fractures. *Journal of Petroleum Technology*. **13** (9), 937–949.

Pruess, K., Oldenburg, C., and Moridis G. 1999. *TOUGH2 User's Guide, Version 2.0. Report LBNL-43134*, Lawrence Berkeley National Laboratory, Berkeley, California.

Rinaldi, A. P., Rutqvist, J., and Cappa, F. 2014. Geomechanical effects on CO2 leakage through fault zones during large-scale underground injection. *International Journal of Greenhouse Gas Control*, **20**: 117–131.

Rutqvist, J., Birkholzer, J.T., Tsang, C.-F., 2008. Coupled reservoir-geomechanical analysis of the potential for tensile and shear failure associated with CO2 injection in multilayered reservoir-caprock systems. *Int. J. Rock Mech. Min. Sci*. **45** (2), 132–143.

Rutqvist, J., Tsang, C.-F., 2002. A study of caprock hydromechanical changes asso-ciated with CO2-injection into a brine formation. *Environ. Geol*. **42**, 296–305.

Rutqvist, J., Y. S. Wu, C. F. Tsang, and G. Bodvarsson. 2002. A modeling approach for analysis of coupled multiphase fluid flow, heat transfer, and deformation in fractured porous rock. *International Journal of Rock Mechanics and Mining Sciences*, **39**: 429–442.

Sayedi, D., Ducellier, A., Foerster, E., Guy, N., Hild, F., and Rohmer, J. 2009. Coupled hydromechanical modeling to study the integrity and safety of geological storage of CO2. *Energy Procedia*, **1**:2451–2458.

Settari, A., Warren, G.M., 1994. *Simulation and Field Analysis of Waterflood Induced Fracturing*. SIMTECH Consulting Services Ltd., Calgary, AB, Canada.

Terzaghi, K. 1936. The shearing resistance of saturated soils and the angle between planes of shear, *Proc. Int. Conf. Soil Mech. Found. Eng*., Vol. **1**, Harvard University Press, Cambridge, MA, 54–6.

Tuminaro, R.S., Heroux, M., Hutchinson, S.A. and Shadid, J.N. 1999. Official Aztec User's Guide Version 2.1. *Massively parallel computing research laboratory*, Sandia National Laboratories, Albuquerque, New Mexico.

van Genuchten, M.T., 1980. A closed form equation for predicting the hydraulicconductivity of unsaturated soils. *Soil Sci. Soc. Am. J*. **44**, 892–898.

Wang W. and Kolditz, O. 2007. Object-oriented finite element analysis of thermo-hydro-mechanical (THM) problems in porous media. *Int J Numer Methods Eng* **69**:162–201

Wibberley C. A. J., Yielding G., and Di Toro, G. 2009. Recent advances in the understanding of fault zone internal structure: A review. *Geological Society (London) Special Publication*, **299**:5–33.

Winterfeld P. H. and Wu Y.-S. 2014. Simulation of CO2 Sequestration in Brine Aquifers with Geomechanical Coupling. *In Computational Models for CO2 Sequestration and Compressed Air Energy Storage*, edited by J. Bundschuh and R. Al-Khoury, Chapter 8, pp. 275–303, New York, NY: CRC Press.

Winterfeld P. H. and Wu Y.-S. 2015. Simulation of coupled thermal-hydrological-mechanical phenomena in porous and fractured media. SPE 173210_MS-MS, presentated at the SPE Reservoir Simulation Symposium held in Houston, Texas, USA, 23–25 February 2015.

Wu Y.-S. and Winterfeld P. H. 2016. Quantitative Characterization of Impacts of Coupled Geomechanics and Flow on Safe and Permanent Geological Storage of CO2 in Fractured Aquifers, Quarterly Report 2 of Year 2. *Quarterly report for DOE Award Number: DE-FE0023305*.

Yew, C. H. and Weng, X. 2016. *Mechanics of hydraulic fracturing, second edition*. Gulf Professional Publishing, Waltham, MA.